Quantum Electronics **47** (11) 992–999 (2017) ©2017 Kvantovaya Elektronika and Turpion Ltd

https://doi.org/10.1070/QEL16401

Equivalent circuit-level model of quantum cascade lasers with integrated hot-electron and hot-phonon effects

H.R. Yousefvand

Abstract. **We report a study of the effects of hot-electron and hot-phonon dynamics on the output characteristics of quantum cascade lasers (QCLs) using an equivalent circuit-level model. The model is developed from the energy balance equation to adopt the electron temperature in the active region levels, the heat transfer equation to include the lattice temperature, the nonequilibrium phonon rate to account for the hot phonon dynamics and simplified two-level rate equations to incorporate the carrier and photon dynamics in the active region. This technique simplifies the description of the electron–phonon interaction in QCLs far from the equilibrium condition. Using the presented model, the steady and transient responses of the QCLs for a wide range of sink temperatures (80 to 320 K) are investigated and analysed. The model enables us to explain the operating characteristics found in QCLs. This predictive model is expected to be applicable to all QCL material systems operating in pulsed and cw regimes.**

Keywords: *quantum cascade lasers (QCLs), equivalent circuit model, hot electron, hot phonon.*

1. Introduction

Quantum cascade lasers (QCLs) are electrically pumped semiconductor lasers based on optical and electronic intersubband transitions (ISTs) between quantised states within the conduction band [1]. The possibility of cascading active regions is a key advantage of QCLs, in which electrons are 'recycled' from period to period as they cascade down the laser structure.

Conventional mid-IR and resonant-phonon THz QCLs exploit the electron–phonon interaction to assist the fast depopulation of the lower lasing level and help to achieve population inversion between the upper and lower laser states. In QCLs, the emission of an optical phonon is the dominant process controlling the electron transport and ISTs in the active region levels [2]. Additionally, the transport in the active region is controlled by ultrafast ISTs and typically requires a bias of several hundred mV per stage at the lasing threshold. Under strong applied electric field, electrons in the active region will be accelerated and gain a large amount of kinetic energy, which leads to the population of hot electrons with an average energy higher than that of the thermal reservoir. Electrons release this excess kinetic energy by exciting other electrons and emitting photons or phonons. Typically, each injected electron generates several (6–10) phonons per cascade stage, where unbalance between phonon generation and decay rates accumulates optical phonons and may produce a nonequilibrium population of optical phonons (hot phonon) [3]. Therefore, the interaction of carriers and optical phonons in QCLs has to be modified substantially to allow for electron temperature and hot-phonon effects. However, to gain a deeper understanding in the QCL designs, the development of a predictive system-level model that accounts for hot electrons and hot phonons is a necessary prerequisite.

In our previous works we have developed the model of Stark-effect roll-over in QCLs to extract the light–current and electric field–current characteristics of the device [4, 5]; however, hot-electron and hot-phonon effects have been neglected. This paper describes a circuit-level implementation of QCLs that includes hot-electron and hot-phonon effects. The total equivalent circuit model is composed of several interactive sub-circuits including an input subcircuit to adopt the current–voltage relationship in the device, an electron-temperature sub-circuit to calculate the electron temperature in the upper and lower laser states, a lattice-temperature sub-circuit to incorporate the self-heating effects in the device, a hot-phonon sub-circuit to model the effect of hot-phonon dynamics and an intrinsic sub-circuit to simulate the carrier and photon dynamics in the active region of the device.

H.R. Yousefvand Department of Electrical Engineering, Islamshahr Branch, Islamic Azad University, Tehran 33147–67653, Iran;
e-mail: hossein@iiau.ac.ir

Received 13 April 2017
Kvantovaya Elektronika **47** (11) 992–999 (2017)
Submitted in English

2. Physics and theory

A simplified schematic of the thermal processes and carrier movement occurring within the QCLs is illustrated in Fig. 1. As shown in the figure, electrons are injected electrically from the injector ground state g into laser upper states 3, and then, the injected electrons can make an optical transition to state 2, or follow other nonradiative scattering paths via phonon emission. In the model, we consider three different temperatures T_E, T_L and T_S, denoting the electron temperature in the active region levels, lattice temperature and heat sink temperature, respectively. It is important to note that the electron temperature T_E is created first in the core of the active region and then transferred to the thermal reservoir through the crystal lattice.

2.1. Generation of hot electrons and hot phonons in QCLs

It is known that the active region of QCLs operates under a strong electrical bias. When a voltage is applied to the device,

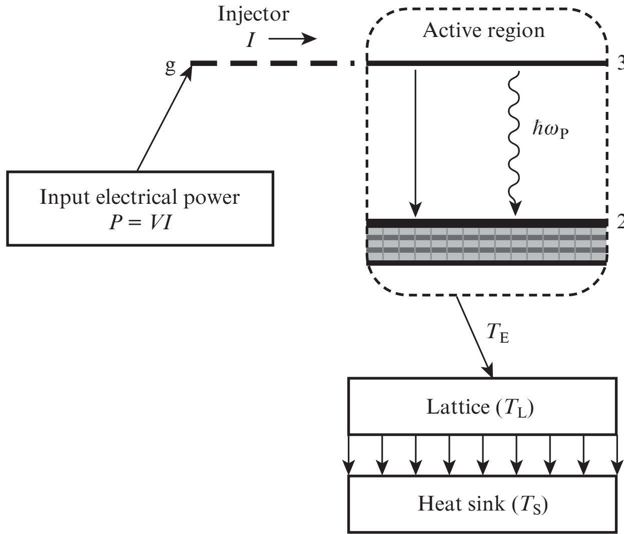

Figure 1. Simplified scheme of the carrier and thermal dynamics within the QCLs.

electrons in the active region will be accelerated and hence gain a large amount of kinetic energy. These energetic electrons are often referred to as hot electrons because the characteristic temperature of these electrons will be much higher than that of the surrounding crystal lattice [6, 7].

The kinetic energy of two-dimensional electrons can be characterised by an effective temperature T_E, which is the same in both the upper and lower laser states [8]. It is worth noting that we should also consistently take into account the dependence of the carrier cooling rate on the effective temperature due to the stimulated photon emission. Therefore, a gain or loss of the total energy of the two-dimensional electrons in the active region can be modelled via a simple rate equation as in our previous work [9]:

$$n_{2D}k_B\frac{\mathrm{d}T_E}{\mathrm{d}t}=\frac{I_T}{eA}(\Delta E_{32}+2\hbar\omega_{LO})$$
$$-n_{2D}k_B\frac{T_E-T_L}{\tau_E}-G\Delta N\frac{N_P\hbar\omega_P}{A}, \quad (1)$$

where I_T is the total current flowing through the device, A is the device area, e is the electron charge, n_{2D} is the surface doping concentration per stage, k_B is the Boltzmann constant, ΔE_{32} is the energy difference between the upper and lower laser states, $2\hbar\omega_{LO}$ is the energy difference between the lower laser state and injector ground state of the next stage, T_L is the lattice temperature, τ_E = 0.22–0.25 ps is the energy loss lifetime between the electron and lattice temperature [7], G is the optical gain, $\Delta N = N_3 - N_2$ is the population inversion difference, N_P is the photon number and $\hbar\omega_P = \Delta E_{32}$ is the photon energy.

On the other hand, heat extraction from QCLs is difficult due to the following reasons: large amount of electrical power P dissipated in the device active regions, poor thermal coupling between the active region and the heat sink caused by the waveguide and mounting configurations and, most importantly, low heat conductivity of the QCL active regions due to theirs superlattice-like nature [10]. Therefore, to model thermal transient processed caused by self-heating and changes in ambient sink temperature, we use the lattice thermal rate equation from our previous work [4]:

$$\tau_{TH}\frac{\mathrm{d}T_L}{\mathrm{d}t}=\sigma(I_TV-P_{out})R_{TH}-(T_E-T_S), \quad (2)$$

where R_{TH} is the thermal resistance, which relates the change in the active region temperature to the power dissipated as heat; τ_{TH} = 1 μs is the thermal time constant determining the heat initially escaping from the active region into the waveguide cladding and isolation layers; P_{out} is the output optical power; σ is the pulse duty cycle; and V is the voltage across the device.

In the following, we still require a correct description for the phonon dynamics inside the device active region. As mentioned above, the imbalance in temperature between the electrons and the lattice necessarily results in the fact that electrons lose some of their kinetic energy to the crystal lattice, thereby creating phonons. Due to the requirement of conservation of energy and momentum during the hot-electron relaxation process, phonons created in this way will have a certain distribution in the momentum space. Therefore, phonons of different wave vectors may have different occupancies; these phonons are not in thermal equilibrium, so they are often called hot phonons or nonequilibrium phonons [6]. For the QCL, where there are many thin layers of heterostructure materials, the dynamical evolution of the electron–phonon system can be described by the coupled Boltzmann equations [2, 11]. However, this is apparently impossible to do numerically. Transport simulations of QCLs generally assume electrons interacting with dispersionless bulk phonons of the well material due to simplicity of the scattering rate calculation under this approximation [12–18]. Furthermore, Williams and Hu [19] showed that the total phonon scattering rates including confinement in one cascade stage (with three quantum wells) of two $GaAs/Al_{0.3}Ga_{0.7}As$ QCLs are very close to those obtained using GaAs-bulk phonons. In view of the setup of our model, this is a reasonable approximation. In this case, the dynamics of the nonequilibrium phonon occupation number and the changing rate of the excess optical phonons with the phonon wave vector $\boldsymbol{q}$ ($|\boldsymbol{q}| = q \approx 0.1$–$0.3\ \mathrm{nm}^{-1}$) can be found from energy conservation condition [6]:

$$\frac{\partial N_q}{\partial t}=\frac{2\pi}{\hbar}(N_q+1)\sum_k|M_q|^2[f_k(1-f_{k-q})\delta(E_{k-q}-E_k+\hbar\omega_{LO})]$$
$$-\frac{2\pi}{\hbar}N_q\sum_k|M_q|^2[f_k(1-f_{k+q})\delta(E_{k+q}-E_k-\hbar\omega_{LO})], \quad (3)$$

where N_q is the phonon distribution function; f_k is the electron distribution function with the wave vector $\boldsymbol{k}$; $\hbar\omega_{LO}$ is the longitudinal optical (LO) phonon energy; $\delta(x)$ is the delta function;

$$|M_q|^2=\frac{2\pi e^2\hbar\omega_{LO}}{V_Lq^2}\left(\frac{1}{\varepsilon_\infty}-\frac{1}{\varepsilon_0}\right) \quad (4)$$

is the square of the modulus of bulk GaAs electron–LO phonon (Frohlich) interaction matrix element; V_L is the volume of one cascade stage; and ε_∞ and ε_0 are the high-frequency and static dielectric constant, respectively. If we assume that the electrons are at quasi-equilibrium obeying a Boltzmann distribution with temperature T_E and that f_k is much smaller

than unity, the excess LO-phonon distribution function N_q generated by hot electron relaxation can be simplified and takes the form [6]:

$$\frac{dN_q}{dt} = \frac{2\hbar\omega_{LO}e^2}{\hbar^2 c V_L}\left(\frac{2\pi^2 m^* c^2}{k_B T_E}\right)\left(\frac{1}{\varepsilon_\infty} - \frac{1}{\varepsilon_0}\right) \times \frac{N_3}{q^3}\left(1 - \frac{N_q}{N_q^0}\right)\exp\left(-\frac{E_{q^2}}{k_B T_E}\right), \quad (5)$$

where $N_q^0 = \{\exp[\hbar\omega_{LO}/(k_B T_L)] - 1\}^{-1}$ is the Bose–Einstein distribution of the equilibrium optical phonons; c is the velocity of light in the vacuum; m^* is the electron effective mass,

$$E_{q^2} = \frac{(E_q + \hbar\omega_{LO})^2}{4E_q}; \quad (6)$$

and $E_q = \hbar^2 q^2/(2m^*)$. Finally, the distribution function of the LO-phonon occupation number, including the equilibrium and nonequilibrium terms, can be expressed as [20]:

$$N_q^n = N_q^0 + \frac{dN_q}{dt}\tau_q, \quad (7)$$

where τ_q (~2–3 ps) is the optical phonon lifetime.

2.2. Current–voltage (I–V) characteristic in QCLs

Electronic transport in QCLs takes place by tunnelling between the injector ground state and the upper state of the lasing transition in adjacent quantum wells. An analytical expression for the tunnelling current between these two states coupled via an injection barrier was derived by describing the system in a tight-binding approach using the density matrix formalism [21]:

$$I_0 = eAn_{2D}\frac{2|\Omega|^2\tau_\perp}{1 + \Delta^2\tau_\perp^2 + 4|\Omega|^2\tau_3\tau_\perp}, \quad (8)$$

where $\hbar\Delta = E_g - E_3 \approx ed(F - F_r)$ is the energy difference between the injector ground state g and the laser upper state 3; F_r is the electric field which brings the states g and 3 in resonance; F is the average electric field applied over the distance d (length of one period); and $\hbar\Omega = 2$ meV is the coupling energy between the states g and 3. The time constant τ_3 represents the LO-phonon scattering lifetime of an electron in the state 3 and $\tau_\perp$ is the relaxation time for the momentum in the plane of the layer, responsible for the loss of phase between the states involved in resonant tunnelling. An estimate for $\tau_\perp$ in the 10–300 K range is 100–50 fs [21]. Unfortunately, in the literature the original derivation for the bias dependence of the injection current expressed by Eqn (8) neglects stimulated emission and is even more valid for below the laser threshold. Therefore, this expression cannot predict the actual device current. To adopt the actual current–voltage relationship of the device for above the threshold, in accordance with conventional interband diode lasers and with a good approximation for QCLs, we assume a linear relation between the device voltage and the device current, as [22]:

$$V = V_{th} + R_d I \ \text{for} \ V \geqslant V_{th}, \quad (9)$$

where V_{th} denotes the device threshold voltage and R_d is the differential resistance. Using the differential series resistance $\partial V/\partial J = 0.00142N + 0.0675$ mΩ cm^2, the voltage drop in each period $\Delta V_P = e^{-1}(E_{32} + E_{21})$ and the threshold current density J_{th}, the voltage at the laser threshold can be estimated as [23, 24]:

$$V_{th} = \left(\frac{E_{32} + E_{21}}{e}\right)N + V_S + \frac{\partial V}{\partial J}J_{th}, \quad (10)$$

where the voltage $V_S = 0.33$ V is due to the series resistance caused by the non-alloyed contacts, graded-gap regions and ungraded-gap regions; $E_{32} + E_{21}$ denotes the energy drop per stage; N is the number of cascade stages. Then, the threshold current density J_{th} can be estimated using the gain coefficient g, the total losses (sum of the mirror loss and waveguide loss: $\alpha_m + \alpha_w$) and the confinement factor $\Gamma = \Gamma_P N = 0.33$ (Γ_P is the overlap factor between the optical mode and one period of the structure) [24, 25]:

$$J_{th} = \frac{\alpha_m + \alpha_w}{\Gamma g}. \quad (11)$$

Knowing the values of the LO-phonon lifetimes τ_3, τ_2 and τ_{32}, the cascade stage length L_P, the optical transition matrix element z_{32}, and the full-width at half-maximum (FWHM) of the luminescence spectrum $2\gamma_{32}$, we calculate the gain coefficient g as [25]:

$$g = \tau_3\left(1 - \frac{\tau_2}{\tau_{32}}\right)\frac{4\pi e z_{32}^2}{\varepsilon_0 n_{eff}\lambda L_P}, \quad (12)$$

where n_{eff} is the effective refractive index of the lasing mode, λ is the laser emission wavelength, and ε_0 is the dielectric constant of the vacuum. After putting $d(F - F_r) \approx (V - V_{th})/N$ into (8), we can estimate the total current flowing through the device:

$$I_T = I_0 + I. \quad (13)$$

This approximation enables us to estimate the value of the device current as a function of applied voltage for below and above the laser threshold.

2.3. Carrier and photon dynamics within the QCL active region

Our physical model describing the carrier and photon dynamics in the QCL active region is based on a two-level classical scheme with three equations: two for electrons on the upper and lower levels involved in the laser transition, and one for the photons in the laser cavity. For a QCL with N cascade stages, simplified rate equations for the electron–photon system have the form [4, 26]:

$$\frac{dN_3}{dt} = \frac{I_T}{e} - \frac{N_3}{\tau_3} - G(N_3 - N_2)N_P, \quad (14)$$

$$\frac{dN_2}{dt} = \frac{N_3}{\tau_{32}} - \frac{N_2}{\tau_2} + G(N_3 - N_2)N_P, \quad (15)$$

$$\frac{dN_P}{dt} = NG(N_3 - N_2)N_P - \frac{N_P}{\tau_P} + N\beta\frac{N_3}{\tau_{SP}}, \quad (16)$$

where β and τ_{SP} are the spontaneous emission coupling coefficient and the spontaneous relaxation time between levels 3 and 2, respectively; τ_P is the photon lifetime;

$$G = \Gamma \frac{c}{V_a} \frac{4\pi e^2 z_{32}^2}{n_{eff}^2 \varepsilon \lambda 2\gamma_{32}(T)}; \tag{17}$$

$V_a = NWLL_P$ is the cavity volume; and W and L are the width and length of the cavity, respectively. Furthermore, the FWHM temperature dependence can be included as [27]:

$$2\gamma_{32}(T) = 2\gamma_{32}(0)(2N_q^n + 1), \tag{18}$$

where $2\gamma_{32}(0) = 10$ meV. In mid-IR QCLs, where the energy distance between the upper and lower laser states is much bigger than the LO-phonon energy, the LO-phonon scattering rates dominate over the electron--electron and other non-radiative scattering processes. Therefore, we assume that the emission and absorption times of a phonon by an electron undergoing a transition between the upper and lower states 3 and 2 are assumed comparable. In this case, the thermal dependence of τ_3 and τ_{32} are approximated as [27,28]:

$$\tau_3^{-1}(T) = \tau_3^{-1}(0)(2N_q^n + 1), \tag{19}$$

$$\tau_{32}^{-1}(T) = \tau_{32}^{-1}(0)(2N_q^n + 1). \tag{20}$$

Due to the design strategies in mid-IR QCLs, in which the energy distance between the lower laser state and the ground state in the active region has been chosen equal to an LO-phonon energy, the emission process dominates over the absorption mechanism. In this approximation we obtain:

$$\tau_2^{-1}(T) = \tau_2^{-1}(0)(N_q^n + 1). \tag{21}$$

3. Circuit-level implementation

Since our goal is to construct a QCL model that addresses the device behaviour by the circuit-level simulation of optoelectronic systems, we try to implement this model in SPICE-like simulators such as HSPICE. The development of our circuit model has several main parts. As shown in Fig. 2, the first part is the input sub-circuit including a general diode, a non-linear voltage dependent current source, a current dependent voltage source, and a series resistance, which implement the QCL current–voltage characteristic defined in Eqn (9). The input sub-circuit receives the bias voltage V as an input and produces the current I_T flowing through the device as an output.

The second part, which originates from the heat transfer equation defined in Eqn (2), is a lattice-temperature sub-circuit that receives the sink-temperature as an input and produces the lattice-temperature as an output. In the lattice-temperature sub-circuit, V_{TL} is the terminal which models the heat transfer equation via the resistance $R_L = R_{TH}$, the capacitor $C_L = \tau_{TH}/R_{TH}$, and a nonlinear current source as:

$$G_L = \frac{T_S}{R_{TH}} + \sigma(I_T V - P_{out}). \tag{22}$$

In the following, to improve the convergence properties of the model, we introduce some transformation for the photon

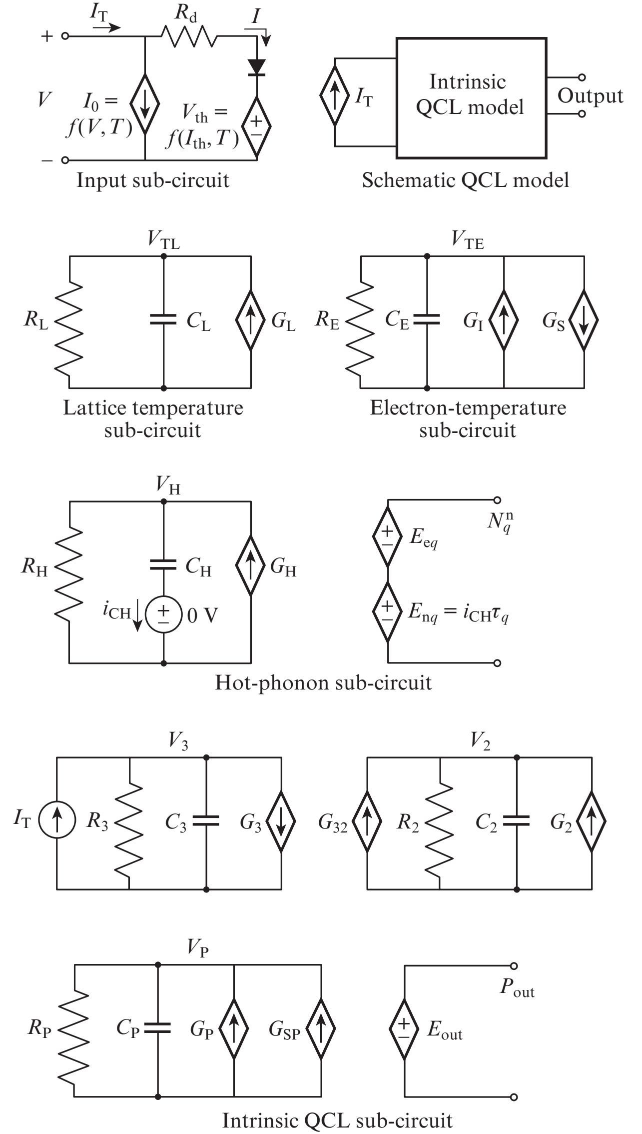

Figure 2. Complete QCL circuit model, including elements for modelling current–voltage characteristics, lattice temperature, electronic temperature, hot-phonon effects and the intrinsic QCL behaviour.

number N_P and the carrier number N_i (i = 2, 3) using the equations [29]:

$$N_i = z_n V_i |_{z_n \approx 10^{15}}, \tag{23}$$

$$N_P = \frac{(V_P + \delta)^2}{k}\bigg|_{k \approx 1.5\times 10^{-19}}, \quad \delta \geqslant 0, \tag{24}$$

where z_n and k are the arbitrary constants.

The third part, which is the electron-temperature sub-circuit, can be obtained by substituting Eqns (23) and (24) into Eqn (1). In the electron-temperature sub-circuit, V_{TE} is the terminal whose node voltage models the electron temperature T_E via the capacitor $C_E = \tau_E$, the resistance $R_E = 1$, and the nonlinear current sources G_I and G_S, as

$$G_I = V_{TL} + \frac{\tau_E I_T}{eAn_{2D}k_B}(\Delta E_{32} + 2\hbar\omega_{LO}), \tag{25}$$

$$G_S = z_n G(V_3 - V_2)\hbar\omega_P \frac{(V_P + \delta)^2}{k} \frac{\tau_E}{An_{2D}k_B}. \quad (26)$$

The fourth part is the hot-phonon sub-circuit that is supported by the balance equation [Eqn (5)]. In the hot-phonon sub-circuit, V_H is the terminal whose node voltage models the hot-phonon dynamics via the capacitor $C_H = 1$, the resistance $R_H = N_q^0/G_H$, and the nonlinear current source

$$G_H = \frac{2\hbar\omega_{LO}e^2}{\hbar^2 c}\left(\frac{2\pi^2 m^* c^2}{k_B V_{TE}}\right)\left(\frac{1}{\varepsilon_\infty} - \frac{1}{\varepsilon_0}\right) \times \frac{z_n V_3}{q^3}\exp\left(-\frac{E_{q^2}}{k_B V_{TE}}\right). \quad (27)$$

Since we are mainly interested in the distribution function of phonons including the equilibrium and nonequilibrium distributions, as defined in Eqn (7), we use a voltage-controlled voltage source ($E_{eq} = N_q^0 = \{\exp[\hbar\omega_{LO}/(k_B V_{TL})] - 1\}^{-1}$) as well as the current-controlled voltage source ($E_{nq} = \tau_q i_{CH}$) to model the phonon dynamics.

The fifth part is the intrinsic QCL sub-circuit that models the carrier and photon rate equations. Substituting Eqns (23) and (24) into Eqns (14)–(16) and applying proper operations, we obtain new equations which can be mapped directly into the intrinsic QCL sub-circuit (by applying Kirchhoff's current law to the sub-circuit nodes).

In the intrinsic QCL sub-circuit, V_3 is the terminal whose node voltage models the electron number N_3 via the capacitor $C_3 = ez_n$, the resistance $R_3 = \tau_3/(ez_n)$, and the nonlinear current source

$$G_3 = \frac{ez_n G(V_3 - V_2)(V_P + \delta)^2}{k}. \quad (28)$$

In the same way, V_2 is the terminal whose node voltage models the electron number N_2 via the capacitor $C_2 = ez_n$, the resistance $R_2 = \tau_2/(ez_n)$, the nonlinear current sources $G_2 = ez_n V_3/\tau_{32}$ and $G_{32} = G_3$. Similarly, V_P is the terminal whose node voltage models the photon number N_P via the capacitor $C_P = 2\tau_P$, the resistance $R_P = 1$, the nonlinear current sources

$$G_P = z_n NG\tau_P(V_3 - V_2)(V_P + \delta) - \delta, \quad (29)$$

$$G_{SP} = k\tau_P \frac{z_n N\beta V_3}{V_P + \delta}. \quad (30)$$

Finally, to calculate the output power P_{out}, we use the voltage-controlled voltage source:

$$P_{out} = E_{out} = \frac{\eta_{out}\hbar\omega_P(V_P + \delta)^2}{k\tau_P}, \quad (31)$$

where η_{out} is the output power coupling efficiency.

4. Results and discussion

While the proposed system-level model is quite general and applicable to different cascade structures, in simulations we consider a typical InP-based mid-IR QCL with the following geometrical and material parameters that are adjusted to describe experimental data [30, 31]: W = 24 μm, L = 2 mm, L_P = 45 nm, N = 30, R_{TH} = 15 K W^{-1}, $\Delta E_{3,2}$ = 150 meV, τ_P = 5 ps, n_{eff} = 3.27, $\tau_3(0)$ = 1.5 ps, $\tau_2(0)$ = 0.2 ps, $\tau_{32}(0)$ = 2.5 ps, and z_{32} = 1.7 nm.

4.1. Steady-state analysis

The light–current characteristic with a duty cycle of 40% (Fig. 3) suggests that the model accurately predicts the degradation of the output power due to the thermal roll-over. Also, one can see that the threshold current is affected by both the sink temperature and pulse duty cycles. Figure 4a demonstrates the thermal roll-over output power versus the total injected current for different duty cycles. One can see that in low duty cycles (less than 20%), the output power dose not exhibit the thermal roll-over for these range of the injected current because the electronic temperature is slightly higher than the lattice temperature that is approximately equal to the sink temperature. At higher duty cycles (above the 20%), the output power obviously illustrates the thermal roll-over because the characteristic temperature of the electrons in the active region will be much higher than that of the surrounding crystal lattice, which does not remain constant in the interval from the laser threshold to the output roll-over. Figure 4b shows the difference between the electronic temperature T_E in the active region and the lattice temperature T_L as a function of the total injected current I_T. When the injected current is increased, the difference between the electronic temperature and the lattice temperature also increases, in agreement with experiment [7].

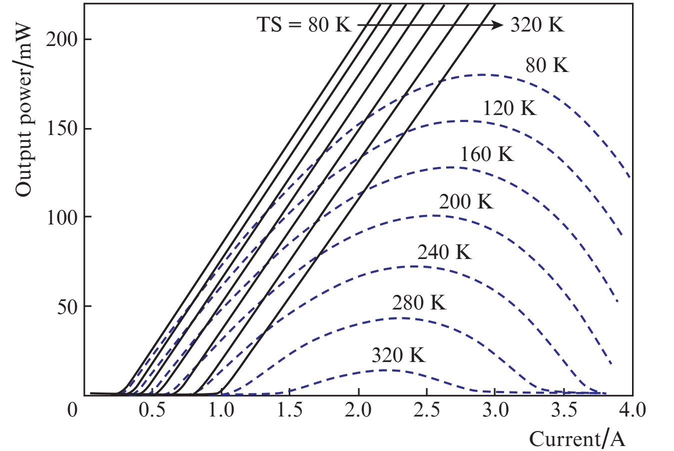

Figure 3. Calculated output powers as a function of total injected current I_T with (solid lines) 1% and (dashed curves) 40% duty cycles for different sink temperatures T_S.

Figure 5a plots the difference between the electronic temperature T_E and the lattice temperature T_L as a function of applied voltage with a 40% duty cycle for a wide range of sink temperatures. One can see that at a low applied bias below the laser threshold (less than 5.5 V), the electronic temperature is approximately equal to the lattice temperature at all sink temperatures. At higher applied voltages above the laser threshold, the difference $T_E - T_L$ is increased, T_E can be approximated as a linear function $T_E \approx T_L + \beta_0 I_T$, where $I_T = V/R_d$ and the parameter β_0 characterises the electron heating rate (in K A^{-1}). As can be seen from Fig. 5a, with increasing sink temperature the slope $\mathrm{d}(T_E - T_L)/\mathrm{d}V$ above

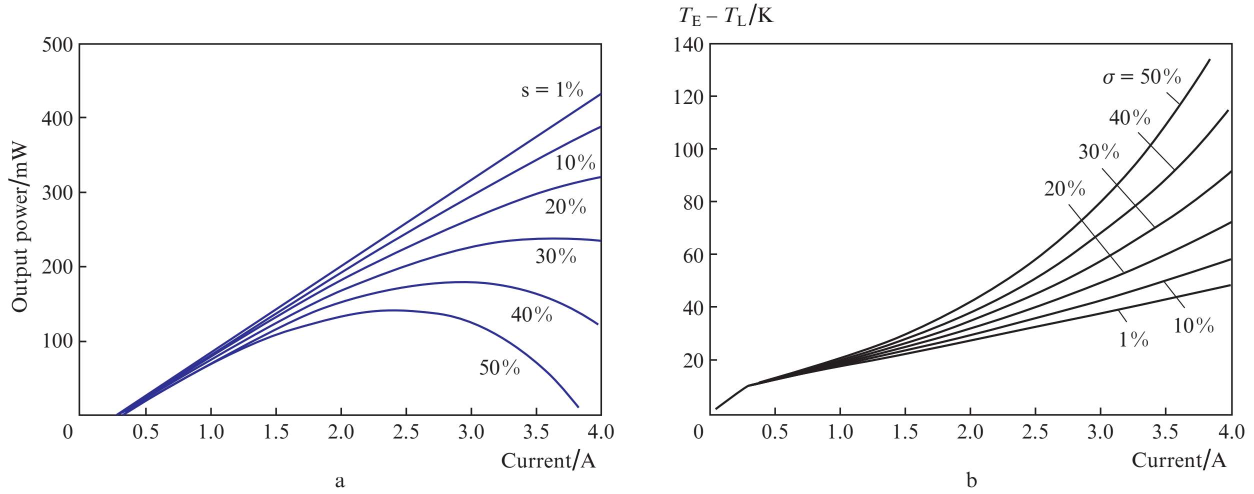

Figure 4. (a) Calculated output power and (b) difference between the electronic temperature of the active region T_E and the lattice temperature T_L as a function of total injected current at $T_S = 80$ K for different duty cycles σ.

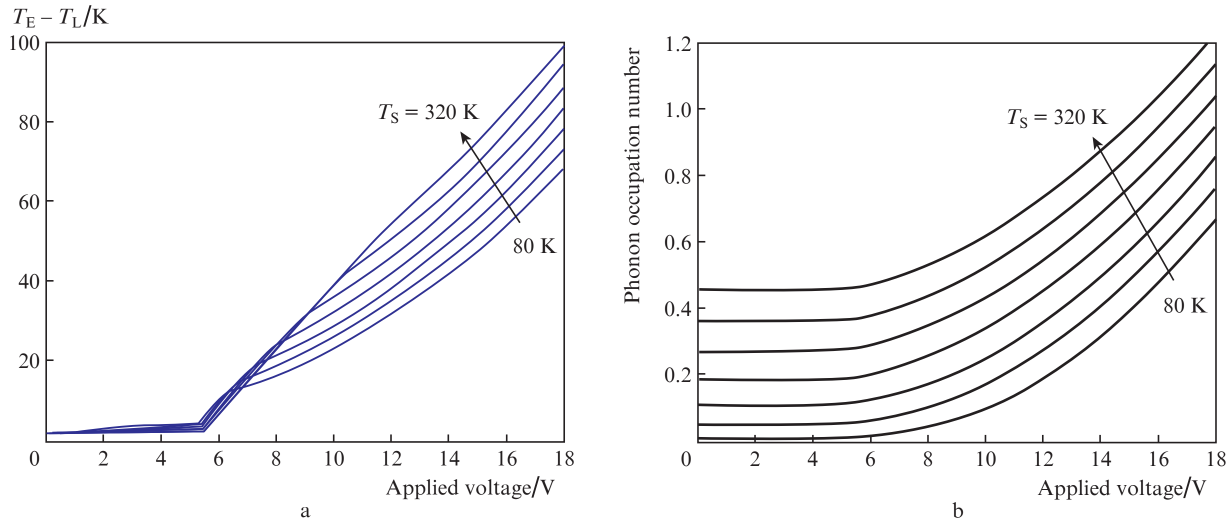

Figure 5. (a) Calculated difference between the electronic temperature T_E and the lattice temperature T_L, and (b) the total phonon occupation number (7) as a function of applied voltage with a 40% duty cycle for heat sink temperatures $T_S = 80$, 120, 160, 200, 240, 280 and 320 K.

the laser threshold progressively increases, meaning that the electron cooling becomes less effective, which is in agreement with the experimental observations [7]. Consequently, the electron heating rate decreases indicating that the photon emission extracts a strong part of the input electrical power, efficiently cooling the electrons. This fact originates from the stimulated photon emission term in Eqn (1) which increases with decreasing sink temperature (see Fig. 3). In Fig. 5b, the total phonon occupation number based on Eqn (7) is shown as a function of the applied voltage for a wide range of sink temperatures. It can be seen that the phonon occupation number is dramatically increased with applied bias, which degrades the device performance.

4.2. Dynamic response

To illustrate the other capabilities of the model, the equivalent circuit is also studied under the transient and small-signal operations. In the transient regime, a pulse train of the rectangular input voltage is chosen which changes from 8 V to 16 V with 1 ns rise and fall times. The pulse duration is 200 ns and their repetition rate is 2 MHz. Figure 6a shows the time dependences of the electron temperature in the active region and of the lattice temperature in the pulsed regime. It can be seen that at the end of the initial period, the lattice temperature has not regained the sink temperature and so the lattice temperature (and subsequently the electron temperature) increases further during the next period. This heat accumulation process (that originates from the input applied voltage for both the lattice and active region temperatures) causes the active region and its surrounding crystal lattice to progressively rise in temperature during each successive pulse until saturation occurs. These results are in agreement with the numerical calculations reported so far [32].

Figure 6b shows the temporary evolution of the phonon occupation number with and without the hot-phonon effect taken into account. The accumulation of the phonon occupation number can be understood from the change of electron

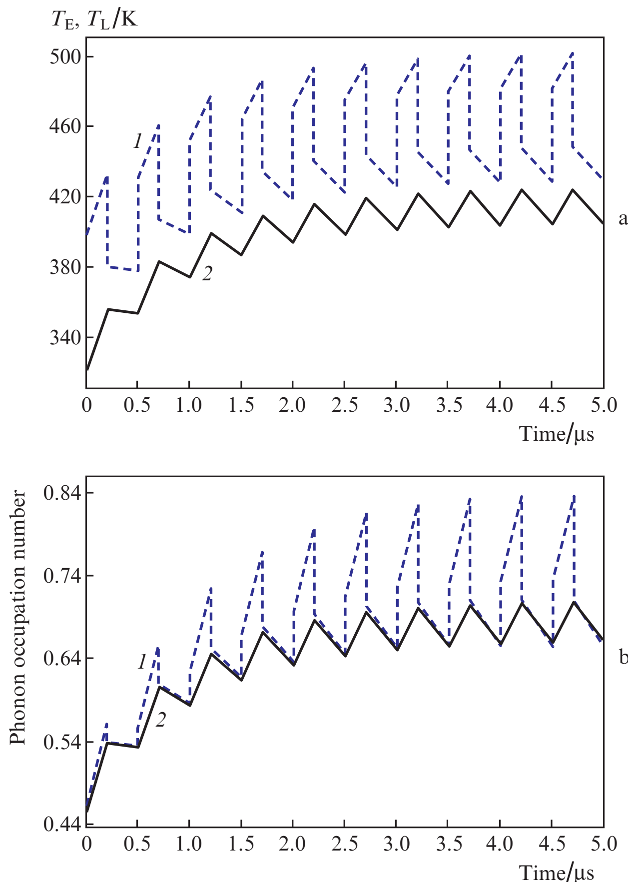

Figure 6. (a) Time dependences of (*1*) electronic and (*2*) lattice temperatures and (b) of the total phonon occupation number (*1*) with and (*2*) without the hot-phonon effect for a 40% duty cycle and T_S = 320 K. The repetition rate of 200-ns voltage pulses is 2 MHz.

and lattice temperatures in response to the input voltage pulses. The results reveal that the induced nonequilibrium phonon emission must play an important role in the device dynamics, which is in agreement with the result calculated by the ensemble Monte Carlo technique [33].

Finally, Fig. 7 depicts the normalised modulation response of the output power versus the modulation frequency for different values of the heat sink temperature under the applied voltage of 8 V. It can be seen that the laser bandwidth is remarkably affected by the self-heating effect at the 40% duty cycle. Another important aspect of the QCL is the nonresonant behaviour of the device's frequency response [29], which originates from the ultrafast ISTs in QCLs. Apparently, the proposed model predicts the nonoscillating behaviour of the modulating frequency response, and once again confirms the validity of the model.

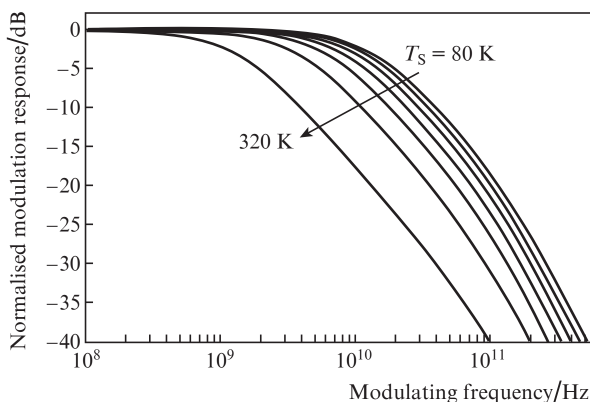

Figure 7. Normalised modulation response of the output power versus the modulating frequency under the applied voltage of 8 V with a 40% duty cycle at heat sink temperatures T_S = 80, 120, 160, 200, 240, 280 and 320 K.

5. Conclusions

Based on a simple equivalent-circuit model, we have presented a detailed theoretical study of hot-electron and hot-phonon effects on the output characteristics of QCLs. For a wide range of heat sink temperatures and under different duty cycles, our model accurately predicts the steady-state and dynamic operating characteristics found in QCLs such as the electronic temperature, the lattice temperature, the output power thermal roll-over and nonresonant behaviour of the modulating frequency response. The results reveal that this predictive model can be a valuable tool for the simulation of QCLs in an optoelectronic device simulator. Furthermore, the model is expected to be applicable to all quantum cascade structures when calculating the cw and pulsed operating characteristics.

Acknowledgements. The author gratefully acknowledge the financial and other supports of this research, provided by the Islamic Azad University, Islamshahr Branch (Tehran, Iran).

References

1. Faist J., Capasso F., Sivco D.L., Sirtori C., Hutchinson A.L., Cho A.Y. *Science*, **264**, 553 (1994).
2. Vitiello M.S., Lotti R.C., Rossi F., Mahler L., Tredicucci A., Beere H.E., Ritchie D.A., Hu Q., Scamarcio G. *Appl. Phys. Lett.*, **100**, 091101 (2012).
3. Scamarcio G., Vitiello M.S., Spagnolo V., Kumar S., Williams B.S., Hu Q. *Physica E*, **40**, 1780 (2008).
4. Yousefvand H.R. *J. Lightwave Technol.*, **34**, 1031 (2016).
5. Yousefvand H.R. *Opt. Commun.*, **395**, 61 (2017).
6. Su Z. *PhD Thesis* (University of Berkeley, 1996).
7. Vitiello M.S., Scamarcio G., Faist J., Scalari G., Walther C., Beere H.E., Ritchie D.A. *Appl. Phys. Lett.*, **94**, 021115 (2009).
8. Harisson P., Indjin D., Kelsall R.W. *J. Appl. Phys.*, **92**, 6921 (2002).
9. Yousefvand H.R. *Appl. Phys. B*, **123**, 137 (2017).
10. Evans C.V., Indjin D., Ikonic Z., Harrison P., Vitiello M.S., Spagnolo V., Scamarcio G. *IEEE J. Quantum Electron.*, **44**, 680 (2008).
11. Shi Y.B., Knezevic I. *J. Appl. Phys.*, **116**, 123105 (2014).
12. Lotti R.C., Rossi F. *Semicond. Sci. Technol.*, **19**, S323 (2004).
13. Callebaut H., Kumar S., Williams B.S., Hu Q., Reno J.L. *Appl. Phys. Lett.*, **84**, 645 (2004).
14. Bonno O., Thobel J.L., Dessenne F. *J. Appl. Phys.*, **97**, 043702 (2005).
15. Gao X., Botez D., Kenzevic I. *Appl. Phys. Lett.*, **89**, 191119 (2006).
16. Jovanovic V.D., Hofling S., Indjin D., Vukmirovic N., Ikonic Z., Harison P., Reithmaier J.P., Forchel A. *J. Appl. Phys.*, **99**, 103106 (2006).
17. Lee S.C., Banit F., Woemer M., Wacker A. *Phys. Rev. B*, **73**, 245320 (2006).
18. Gao X., Botez D., Kenzevic I. *J. Appl. Phys.*, **101**, 063101 (2007).
19. Williams B.S., Hu Q. *J. Appl. Phys.*, **90**, 5504 (2001).
20. Dommelen P.V., Muensit N. *Chin. J. Phys.*, **52**, 1825 (2014).

21. Sirtori C., Capasso F., Faist J. *IEEE J. Quantum Electron.*, **34**, 1722 (1998).
22. Razeghi M. *IEEE J. Sel. Top. Quantum Electron.*, **15**, 941 (2009).
23. Gmachl C., Capasso F., Tredicucci A., Sivco D.L., Kohler R., Hutchinson A.L., Cho A.Y. *IEEE J. Sel. Top. Quantum Electron*., **5**, 808 (1999).
24. Gmachl C., Capasso F., Tredicucci A., Sivco D.L., Kohler R., Billargeon J.N., Hutchinson A.L., Cho A.Y. *Mater. Sci. Eng. B*, **75**, 93 (2000).
25. Gmachl C., Faist J., Capasso F., Sivco D.L., Hutchinson A.L., Cho A.Y. *IEEE J. Quantum Electron*., **34**, 89 (1997).
26. Haldar M.K. *IEEE J. Quantum Electron.*, **41**, 1349 (2005).
27. Hamadou A., Thobel J.L., Lamari S. *Opt. Commun.*, **281**, 5385 (2008).
28. Sirtori C., Page H., Becker C., Ortiz V. *IEEE J. Quantum Electron.*, **38**, 547 (2002).
29. Yousefvand H.R., Ahmadi V., Saghafi K. *J. Lightwave Technol.*, **28**, 3142 (2010).
30. Gmachl C., Capasso F., Sivco D.L., Cho A.Y. *Rep. Prog. Phys*., **64**, 1533 (2001).
31. Faugeras C., Forget S., Duchemin E.B., Page H., Bengloan J.Y., Parillaud O., Calligaro M., Sirtori C., Giovannini M., Faist J. *IEEE J. Quantum Electron.*, **41**, 1430 (2005).
32. Evans C.A., Jovanovic V.D., Indjin D., Ikonic Z., Harrison P. *IEEE J. Quantum Electron.*, **42**, 859 (2006).
33. Paulavicius G., Mitin V., Stroscio M.A. *J. Appl. Phys.*, **84**, 3459 (1998).